

Emergent Nonperturbative Universal Floquet Localization

Soumadip Pakrashi,¹ Atanu Rajak,² and Sambuddha Sanyal¹

¹*Department of Physics, Indian Institute of Science Education and Research (IISER) Tirupati, Tirupati - 517507, Andhra Pradesh, India*

²*Department of Physics, Indian Institute of Technology, Hyderabad 502284, India*

(Dated: January 16, 2026)

We show that a robust, nonperturbative localization plateau emerges in periodically driven quasiperiodic lattices, independent of the static localization properties and drive protocol. Using exact Floquet dynamics, Floquet perturbation theory, and optimal-order van Vleck analysis, we identify a fine-tuned amplitude-to-frequency ratio where all Floquet states become localized despite dense resonances. The van Vleck expansion achieves supersymptotic accuracy up to an optimal order; it ultimately breaks down due to resonant hybridization at a weak quasiperiodic potential, revealing that the observed localization is nonperturbative.

Introduction The localization phenomenon [1] of matter waves due to broken crystalline translation symmetry is one of the most intriguing phenomena in modern physics. In a tight-binding model, localization arises from suppression of the coherent superposition of localized Wannier orbital wavefunctions caused by sufficiently large differences in on-site potentials relative to the hopping amplitude. This insulating regime can be "melted" by a time-periodic drive that can restore the Wannier wave function hybridization [2, 3]. Conversely, localization can also be dynamically engineered in a clean tight-binding model [4] by special time-periodic drive protocols at resonant frequencies, via tuning a destructive interference of the extended wave functions.

Over the past three decades, the idea of engineering localization by tuning the hybridization of Wannier orbitals using time-periodic drives has attracted significant interest [5–7]. In low-dimensional systems, even infinitesimal deviations from crystalline symmetry can lead to complete localization. However, in many practical settings—such as mesoscopic systems [8], engineered optical lattices [9, 10], or materials with broken crystalline order—wavefunctions may instead exhibit partial localization, multifractality, or even coexist as a mixture of localized and delocalized states, separated by a mobility edge. This motivates a central question: *is it possible to engineer complete localization using an external time-periodic drive, regardless of a system's static properties?*

In this Letter, we identify a universal dynamical localization regime that emerges under staggered, time-periodic modulation of the hopping amplitudes in tight-binding models with crystalline symmetry-breaking on-site potential, where the universal localization regime doesn't depend on the properties of the static Hamiltonian or the nature of the drive. Using Van Vleck perturbation theory (VVPT) [11] up to optimal order [12], we characterize the perturbative signatures of this universal localization transition. We find that the effective Floquet Hamiltonian contains algebraically decaying long-range hopping terms whose amplitudes inherit spatial modulations from the underlying onsite potential. The competition between these drive induced long-range modulated

photon-assisted tunneling, and the photon-dressed onsite potential gives rise to a novel, robust localized phase. We further find that due to resonant hybridization, the perturbation theory doesn't capture the universal localization observed in the exact calculation at resonant energies. Those resonant energies are rare when the unperturbed Hamiltonian has a point spectrum or even a multifractal spectrum, but when the unperturbed Hamiltonian has a continuous spectrum, the resonances proliferate across the entire spectrum and the perturbation theory fails to converge. We demonstrate that universal localization is a novel non-perturbative phenomenon that occurs through an interplay of drive and disorder, leaving an impression on a supersymptotic perturbation theory.

Model We consider a tight-binding model with staggered, time-periodic modulation of the hopping amplitudes, described by the Hamiltonian

$$H(t) = \sum_{\langle ij \rangle} (\gamma + a\mathcal{F}(t)) c_{i,A}^\dagger c_{i,B} + (\gamma - a\mathcal{F}(t)) c_{j,A}^\dagger c_{j,B} + \sum_i \left(V_{i,A} n_{i,A} + V_{i,B} n_{i,B} \right) + \text{h.c.} \quad (1)$$

Due to the staggered nature of the drive, it is convenient to write it in a unit cell with a two-site basis, the Hamiltonian in Eq. (1) represents a lattice of \mathcal{N} unit cells consisting of two sublattices (A, B), where i, j represent the unit cell. Alternatively one can also consider uniform drive and staggered hopping [13, 14]. Here $c_{i,A}^\dagger$ creates a particle on sublattice site A in unit cell i , and $n_{i,A}$ is the corresponding number operator. The hopping modulation is governed by a time-periodic function $\mathcal{F}(t)$, with $\mathcal{F}(t+T) = \mathcal{F}(t)$. We consider two representative drive protocols: (i) a sinusoidal drive, $\mathcal{F}(t) = \sin(\omega t)$, and (ii) a square wave pulse alternating between ± 1 over half-periods.

The onsite potential $V_{i,A/B}$ is a crystalline symmetry-breaking potential that varies from site to site. In this letter, we consider the one-dimensional Aubry-Andre model [15] with quasiperiodic potential and its generalizations [16, 17] as primary examples. The Aubry-Andre model is defined as $V_{i,A}^{AA} = \lambda \cos(2\pi\alpha(2i))$, $V_{i,B}^{AA} =$

$\lambda \cos(2\pi\alpha(2i+1))$ in Eq. (1). For generalized Aubry-Andre model $V_{i,A}^{GAA} = 2\lambda \frac{1-(\cos(2\pi\alpha(2i)))}{1+\beta(\cos(2\pi\alpha(2i)))}$, $V_{i,B}^{GAA} = 2\lambda \frac{1-(\cos(2\pi\alpha(2i+1)))}{1+\beta(\cos(2\pi\alpha(2i+1)))}$. In the Aubry-André model, all eigenstates undergo a transition from delocalization to localization as λ increases, passing through a critical point at $\lambda_c = 2$, where all eigenstates are critical. On the other hand, in the generalized Aubry-André (GAA) model, the localization transition occurs through a mobility edge for a range of values of λ and β . The Aubry-André (AA) model and the generalized Aubry-André model are considered as archetypal models of localization transitions in one dimension, which allow computational tractability. However, we argue that the drive-induced universal localization phenomenon is not limited to quasiperiodic or lower-dimensional systems.

Exact results: We first study our model in Eq. (1) using asymptotically exact numerical calculations of the Floquet operator $U(T, 0)$ (details given in the End Matter). The Floquet eigenstates are simultaneous eigenkets of the Floquet operator and the Floquet Hamiltonian H_F , which are related by the equation $U(T, 0) = e^{-iH_F T}$.

To measure localization of the individual Floquet eigenstate, we consider Inverse Participation Ratio (IPR), defined as $\text{IPR}(m) = \frac{\sum_i (\chi_i^m)^4}{(\sum_i (\chi_i^m)^2)^2}$, where χ_i^m denotes the m -th Floquet eigenstate and i indicates the lattice site. For a completely delocalized/extended state, $\text{IPR}(m) \sim 1/L$, where L is the size of the system, whereas, for a completely localized state, IPR is independent of system size. To demonstrate the universal dynamical localization in a compact form, we show a density plot (in Fig. 1(a)) of geometric mean of the IPR ($\langle \text{IPR} \rangle_g$) of all the Floquet eigenstates, for the parameters $\lambda = 1, 2, 3$ for AA model and $(\lambda, \beta) = (-0.8, 0.5)$ for GAA model, as a function of the driving parameters a and ω considering sinusoidal, and square pulse driving protocols, and $\alpha = \frac{\sqrt{5}+1}{2} + \frac{\sqrt{13}+3}{2}$. We observe a region around $a = 1$ and $\omega = 2$, where $\langle \text{IPR} \rangle_g$ has non-zero values, indicating a universal dynamical localization.

We further plot the scaling of IPR with system size for each individual eigenstate in the universal localization region, as well as at a few nearby points for different parameters of the AA and GAA models under different drive protocols. In Fig. 1(c), we find that the IPRs of all the eigenstates at $(a, \omega) = (1, 2)$ for different system sizes collapse for all the cases with $\lambda = 1, 2$ and 3 of the AA model using a sinusoidal driving protocol, thus confirming complete localization. Furthermore, we find that all eigenstates are localized for both square and sinusoidal driving protocols for AA model at $(a, \omega) = (1, 2)$ and $\lambda = 1$, as well as at $(\lambda, \beta) = (-0.8, 0.5)$ for GAA (see Fig. 1(d)). In Figs. 1(e) and 1(f), we plot the system-size scaling of the IPR for all eigenstates at $\lambda = 1$, around the universal localization regime (at the points marked in Fig. 1(a)), and we find that all the eigenstates are delocalized in this region.

Next we compute the spatiotemporal spread of a wavepacket at stroboscopic times ($\psi_{nT}(j)$) that was initially

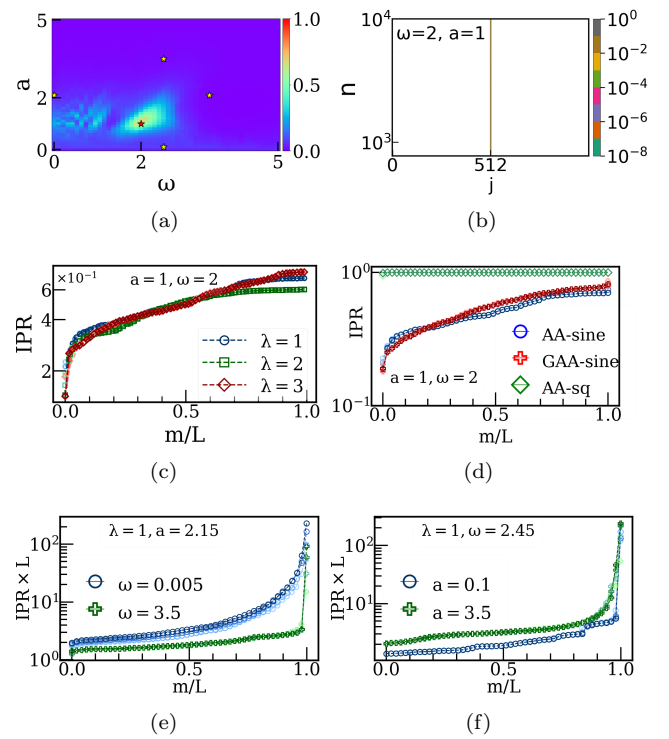


FIG. 1: **a)** $\langle \text{IPR} \rangle_g$ (in color code) is plotted for all Floquet eigenstates χ^m at $\lambda = 1, 2, 3$ of AA model and $(\lambda, \beta) = (-0.8, 0.5)$ of GAA model for both sinusoidal and square wave drive protocols, for $L = 512, N = 200$. A universal localization regime is found near $(a, \omega) = (1, 2)$. **b)** The density plot of the local probability $\langle p_{nT}(j) \rangle_g$ for same parameter values, models, and drive protocols. **c)** $\mathcal{O}(1)$ IPR scaling is observed at $(a, \omega) = (1, 2)$ for AA at $\lambda = 1, 2, 3$, **d)** The same $\mathcal{O}(1)$ scaling is seen across different driving protocols (square/sine pulses) and models (AA: $\lambda = 1$; GAA: $(\lambda, \beta) = (-0.8, 0.5)$). **e),f)** For AA: $\lambda = 1$, $\text{IPR} \sim 1/L$ for points lying outside the localized patch marked by yellow \star in phase diagram 1(a) (Ballistic transport behavior of those regions shown in Fig.3 of supplementary section). Here, $L = 500, 1000, 1500$ and 2000 , the trotter steps $N = 500$, and sinusoidal drive is used for scaling plots. In IPR scaling plots, states are organized in ascending order of IPR magnitude.

localized at the centre of the lattice, where $|\psi(nT)\rangle = U(T, 0)^n |\psi_{\text{in}}\rangle$, ψ_{in} referring to the initial wave packet. In Fig. 1(b), we show the density plot of the local probability $p_{nT}(j) = |\psi_{nT}(j)|^2$ at the universal localization region, as indicated in Fig. 1(a), obtained by taking the geometric mean($\langle p_{nT}(j) \rangle_g$) of the same parameters and drive protocols. We find that, in universal localization regime, the dynamics is completely frozen. The exact numerical results show that the universal localization regime in the amplitude-frequency plane of quasiperiodic chains with staggered driving is independent of both the localization properties of the static counterpart of the model

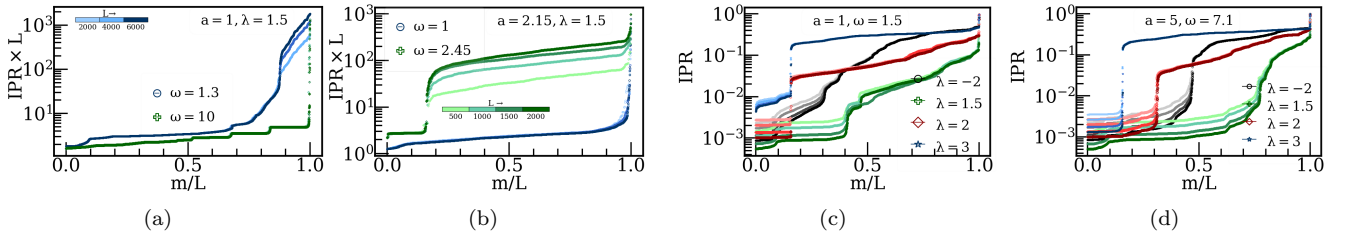


FIG. 2: **a)** Using 2nd order VV, some eigenstates are found to be localized at $\omega = 1.3$ for $a = 1, \lambda = 1.5$, while the revival of high frequency delocalized static limit is seen at $\omega = 10$. **b)** Equivalent localized behavior can be depicted using FPT at $a = 2.15, \omega = 2.45$; while at low frequencies $\omega = 1$ the FPT suggests retrieved delocalized phase. **c),d)** Heuristic extrapolation of VVPT up to an optimal order reveals enhanced localization achieved at $a = 1, \omega = 1.5$ universal localization region compared to $a = 5, \omega = 7.1$ distant regions. Here, $L=1500, 2000, 3000, 4000$ are used for (c)-(d) IPR scaling and sine drive is considered throughout this analysis. In all plots, states are organized in ascending order of IPR magnitude.

and the nature of the drive. However, it is important to note that the universal localization arises from an interplay between disorder and periodic driving; even for $\lambda \rightarrow 0$ (shown in the Fig.3 of Supplementary Material), the universal localization persists, but it does not appear at $\lambda = 0$. We study the detailed mechanism of this interplay using a supersymptotic perturbative approach.

Perturbative approaches We now turn to construct an effective time-independent Hamiltonian governing stroboscopic dynamics of the system using perturbative approaches. We employ Van Vleck perturbation theory (VVPT), that systematically incorporates virtual processes arising from the time-periodic drive by expanding the full Hamiltonian in eqn. 1 in powers of $\frac{1}{\omega}$. VVPT is drive phase independent and gives a Floquet Hamiltonian in real space which can be directly used to study real space dynamics. The effective Hamiltonian in VVPT is given by $H_{eff} = \sum_{n=0}^{\infty} \frac{H^{(n)}}{\omega^n}$, the $H^{(n)}$ terms are given by $H^{(0)} = H_0, H^{(1)} = \sum_{p \neq 0} \frac{[H_{-p}, H_p]}{2p}$, and $H^{(2)} = \sum_{p \neq 0} \frac{[[H_{-p}, H_0], H_p]}{2p^2} + \sum_{p \neq 0, q \neq 0, p} \frac{[[H_{-p}, H_p-q], H_q]}{3pq}$, where, $H_p = \frac{1}{T} \int_0^T e^{-ip\omega t} \hat{H}(t) dt$, and H_0 is the static part of the Hamiltonian in Eq. 1. At order n , the Van Vleck effective Hamiltonian consists of a sum over all nested commutators involving $n+1$ Fourier components of the full Hamiltonian in Eq. 1. These components are constrained by harmonic conservation (i.e., total harmonic index sums to zero), and their nested structure corresponds to distinct bracketings[18, 19]. For drive protocols used in this letter, H_p vanishes for $p \in 2\mathbb{Z} \setminus \{0\}$. From Eq. 1, we get $H_p = \sum_j \mathcal{A}(c_{j,A}^\dagger c_{j,B} - c_{j,A}^\dagger c_{j-1,B} + h.c.)$. For sinusoidal and square drives, $\mathcal{A} = \frac{a}{2i}$ ($p \in 1$) and $\frac{2ia}{p\pi}$ ($p \in 2\mathbb{Z} + 1$), respectively. For $p = 0$, the time-dependent parts of full time-periodic Hamiltonian in Eq. 1 gets integrated to zero and one gets back the static Hamiltonian H_0 . The Fourier components of the time-dependent Hamiltonian (Eq. 1), denoted by H_p , satisfy the relation $H_{-p} = (-1)^p H_p$; consequently, $[H_p, H_{-p}] = [H_{-p}, H_{p-q}] = 0$.

From the properties of H_p , $\mathcal{O}(1/\omega)$ terms in H_{eff} vanish, and at $\mathcal{O}(1/\omega^2)$ only the $[[H_{-p}, H_0], H_p]$ term contributes, which, for the sinusoidal drive, is given by

$$H_2 = -\frac{a^2 \gamma}{\omega^2} \sum_j \left[c_{j,A}^\dagger c_{j-1,B} + c_{j,A}^\dagger c_{j,B} - c_{j+2,A}^\dagger c_{j,B} - c_{j,A}^\dagger c_{j+1,B} - \frac{\lambda}{4\gamma} (2\mathcal{C} n_{j,A} + 2\mathcal{D} n_{j,B} + \mathcal{C} c_{j,A}^\dagger c_{j+1,A} + \mathcal{C} c_{j,B}^\dagger c_{j-1,B}) + h.c. \right]. \quad (2)$$

Here, $\mathcal{C} = \partial_j^2 \cos(2\pi\alpha(2j))$, and $\mathcal{D} = \partial_j^2 \cos(2\pi\alpha(2j+1))$, where the second-order lattice derivative is defined as $\partial_j^2 f(j) \equiv f(j+1) + f(j-1) - 2f(j)$.

Truncating the effective Hamiltonian $H_{VV}^{(2)} = H_0 + H_2$ at $\mathcal{O}(\omega^{-2})$ is a valid approximation when $\omega \gg a$; however, as one approaches $\omega \rightarrow a$ limit, the nearest-neighbor hopping term of H_2 effectively cancels with the nearest-neighbor hopping term in H_0 . At that point, the H_{eff} has a dominant second-neighbor hopping, consisting a pure hopping, and a quasiperiodic hopping in which the quasiperiodic modulation is a linear combination of quasiperiodic potentials of neighboring sites (\mathcal{C}, \mathcal{D}), with a prefactor λ . Moreover, same linear combination of quasiperiodic potential at neighboring sites (\mathcal{C}, \mathcal{D}) also contributes in the onsite potential of the $H_{VV}^{(2)}$. The modulated hopping and onsite potential has the same pre-factor λ , the spectrum of the effective second-order Hamiltonian is expected to have both localized and delocalized states [20], where the localized states appear around $E \sim \omega$, independent of λ . This description remains same for a square drive with appropriate modifications in the prefactors.

We compute the eigenvalues and eigenvectors of effective Hamiltonian $H_{VV}^{(2)}$, and analyse the scaling properties of the IPR from the eigenstates in Fig. 2(a). In Fig. 2(a) we set $\lambda = 1.5$ where all eigenstates are delocalized in the absence of drive, when sinusoidal drive $\mathcal{F}(t)$ is applied with $a = 1, \omega = 10$ we find all the eigenstates are delocalized, as we decrease the frequency of drive to

$\omega = 1.3$ we find that few eigenstates are localized near $E \sim \omega$.

We further probe this localization transition from the low-frequency side. In this limit, we employ the Floquet perturbation theory (FPT) [21] (details given in the End Matter) where the time-dependent part is considered as the unperturbed Hamiltonian and the time-independent part is considered as the perturbation. FPT is valid when $a \gg \lambda, \forall \omega$. In Fig. 2(b), we plot the system-size scaling of the IPR for $a = 2.15, \lambda = 1.5$ at driving frequencies $\omega = 1$ and 2.45 . Both perturbative approaches suggest that, at intermediate amplitudes and frequencies ($a \sim 1 - 2.15$ and $\omega \sim 1.3 - 2.5$), only a subset of eigenstates becomes localized, indicating a reentrant transition analogous to that found in the exact calculations. In contrast to the exact case, the localization region here contains only a few localized states rather than all eigenstates. However, using perturbative approaches, we find indications of localization of the Floquet states in the vicinity of the exact localization regime shown in Fig. 1(a). Notably, in the universal localization region, the first-order FPT Hamiltonian ($H_F^{(1)}$) in position basis, shows a stronger weight in the diagonal terms compared to the off-diagonal term, which in turn promotes the signature of localization (details given in the Fig.4 of supplementary material).

Next we construct an ansatz for the time-independent Floquet Hamiltonian upto an arbitrary order using the recursive structure [22] of Van-Vleck perturbation theory. The commutative structure of successive higher order terms ensures that if the H_0 is quadratic, at an arbitrary order the H_{eff} remains quadratic. The Van-Vleck perturbation expansion is a supersasymptotic series that needs to be truncated at an optimal order $n_*(a, \omega, \lambda, \gamma)$ [12, 19, 23–26]. The truncation criteria is determined by a ratio test of the appropriate norm of the H_{eff} in successive order[27].

In this letter we will focus on H_{eff} for sinusoidal drive only (without loss of any generalities), where $p \in 1$. For this discussion, we split the $H(t)$ into the kinetic term $H_h^0 = \gamma \sum_{\langle ij \rangle} c_{i,A}^\dagger c_{i,B} + h.c.$, static potential term $H_v^0 = \sum_i V_{i,A} n_{i,A} + h.c.$ and time-dependent drive $H_v = \mathcal{F}(t) \sum_{\langle ij \rangle} c_{i,A}^\dagger c_{i,B} + h.c.$. In order to construct the ansatz Hamiltonian, we use two important structures of the nested commutators as follows: 1) all odd order terms in the series vanishes due to the property $H_{-p} = (-1)^p H_p$. 2) From the harmonic sum conservation of a time-independent Floquet Hamiltonian, one can create the $2k+2$ -th order term from the $2k$ -th order term by adding two H_0 in the nested commutators, or by adding H_1 and H_{-1} , and then permuting the combination. This property keeps the number of terms tractable as a branching tree [18, 19]. The final effective Hamiltonian will have three types of terms at $\mathcal{O}(1/\omega^{2k})$. First: pure hopping terms that connect maximum up to $2k+1$ -th neighbors generated by nested commutators H_h^0 and $H_{\pm 1}$ terms, due to the H_{-1} term, the hopping ampli-

tude between neighbors closer than $2k+1$ distance will be an oscillatory sum of the amplitudes of all the processes. Second: hopping terms that connect maximum up to $2k$ -th neighbors generated by nested commutators of H_h^0, H_v^0 and $H_{\pm 1}$ terms, since this is a hopping mediated by the H_v^0 term, this will contain the quasiperiodic potential. The H_v^0 mediated hopping terms will have the structure of a higher order lattice derivative and depending on the $i - j$ -value it flips the sign of hopping. Third: Onsite potential terms generated by the combined action of $H_{\pm 1}, H_v^0$ and H_h^0 , representing particle's return to origin. This combination of $H_{\pm 1}, H_v^0$ and H_h^0 processes also sets the total power associated with hopping amplitudes $\mathcal{Z} = \tilde{p} + \tilde{q}$, which further decides the order of lattice derivative, while remaining power $\tilde{r} = 2\tilde{m} + 1 - \mathcal{Z}$ represents products of cosine harmonics. Considering all these processes, we construct an effective Floquet Hamiltonian at an arbitrary order of perturbation theory as following,

$$H_{eff} = \sum_{i,j} \left(\delta_{|i-j|,0} \lambda \cos(2\pi\beta j) + \delta_{|i-j|,1} \gamma + R_{i,j}^{2k} \right) c_i^\dagger c_j + h.c.. \quad (3)$$

where

$$R_{i,j}^{2k} = \sum_{\substack{\tilde{m}=1,2,3 \\ |i-j| \in I_{\tilde{m}}}}^k \left(\frac{1}{\omega} \right)^{2\tilde{m}} \left[\sum_{\tilde{p}=2,4,\dots}^{2\tilde{m}} \chi \left(\frac{a}{2} \right)^{\tilde{p}} \right. \\ \times \left. \sum_{\substack{\tilde{q}=|i-j|-\tilde{p}+2\tilde{l} \\ \tilde{l}=0,1,2,\dots \\ \tilde{q} \geq 0, \tilde{r}=2m+1-\tilde{p}-\tilde{q}}}^{2\tilde{m}+1-\tilde{p}} (\lambda f)^{\tilde{r}} \gamma^{\tilde{q}} \zeta_{\tilde{m},\tilde{p},\tilde{q},\tilde{r},|i-j|} \right], \quad (4)$$

$I_1 = [0, 3], I_2 = [0, 5], I_3 = [0, 7] \dots$. Here $\zeta_{\tilde{m},\tilde{p},\tilde{q},|i-j|} = (-1)^{\frac{|i-j|+1}{2}}$ when $(\tilde{p}, \tilde{q}) = (2\tilde{m}, 1)$, otherwise $\zeta_{\tilde{m},\tilde{p},\tilde{q},|i-j|} \in \{\pm 1\}$, taken randomly to mimic the sign flips for H_{-1} mediated processes, however we note that this sign is not very important given that it multiplies an oscillating trigonometric factor. To match with Eq. 2 the prefactor χ is chosen as $\chi=4$ for $|i-j|=1, 3$ at $(\tilde{p}, \tilde{q}) = (2\tilde{m}, 1)$, $\chi = 2$ for $|i-j|=0$ and $\chi=1$ otherwise. $f = \partial^{\mathcal{Z}} f(i,j) = \sum_{\tilde{r}=0}^{\mathcal{Z}} (-1)^{\tilde{r}} \binom{\mathcal{Z}}{\tilde{r}} \cos(2\pi\beta(c + \tilde{r} - \frac{\mathcal{Z}}{2}))$, where $c = \frac{i+j}{2}$. The closed-form analytical expression of $R_{i,j}^{2k}$ (Eq. 5) is obtained by a heuristic extrapolation of the lower order terms.

Here each real-space term $R_{i,j}^{(2k)}$ is a sum over virtual processes in the H_0 basis and hence equals a sum of products of matrix elements divided by detunings. Resonant divergences occur when one (or a product) of these denominators becomes anomalously small; thus the perturbation theory can only be used away from these resonances i.e. when the drive frequency matches the difference between unperturbed Hamiltonian eigenenergies. At lower values of λ , the spectrum becomes continuous, leading to a complete breakdown of the perturbation theory throughout the spectrum due to resonance proliferation. We determine the optimal order truncation of the

superasymptotic VVPT by ratio test, $\bar{R}^{2k+2}/\bar{R}^{2k} < 1$, where $\bar{R}^{2k} = \langle |R_{i,j}^{2k}| \rangle_{ij}$ [27]. Despite the resonances, the ratio test remains well-behaved; we also discuss the other norms [27] in the Sec:3 of supplementary material.

In Figs. 2(c) and 2(d), we plot the IPR scaling at the optimal order of truncation of VVPT at $(a, \omega) = (1, 1.5)$ and $(5, 7.1)$, which is at the universal localization and away from it, respectively. The ratio test results for these two cases are shown in the supplementary section 3. From the IPR scaling, we find that more states are localized in the universal localization region than away from it. The difference is more clear from $\lambda = 1.5$ and $\lambda = 2$, in Figs. 2(c) and Fig. 2(d), where all eigenstates are delocalized and critical states without drive, respectively, and also in the case of GAA with mobility edge. Note that all the cases have resonant energy states in the spectrum, these are not the mobility edges, these resonances increase more as the spectrum gets continuous at lower λ and the perturbation theory fails to explain the localization (Fig. 1(c)).

Conclusion In summary, we have demonstrated the existence of a robust, non-perturbative localization phenomenon in periodically driven quasiperiodic lattices. Using exact Floquet dynamics, Floquet perturbation theory and Van-Vleck (VV) asymptotic expansions, we identified a region in the amplitude–frequency plane at which all Floquet eigenstates become localized irrespective of the properties of the undriven Hamiltonian. Although the Van-Vleck expansion is divergent, its optimally truncated form accurately captures the non-resonant part of the Floquet spectrum. The resulting agreement with exact results suggests that a fundamentally non-perturbative localization mechanism leaves an imprint on a divergent perturbative series. We further showed that the eventual breakdown of the superasymptotic VV series originates from rare, large resonant hybridizations that are invisible to global ratio tests but dominate the physical long-range couplings. This dichotomy between bulk asymptotic behavior and sparse resonances provides a single-particle analog of the rare-resonance-induced collapse of the Floquet-Magnus expansion known in many-

body systems [12, 19, 23, 26, 28].

The non-perturbative universality of the localization plateau persisting across quasiperiodic potentials, drive protocols, and parameter ranges suggests that this phenomenon is not restricted to only quasiperiodic model and is likely to extend to higher dimensions and even disordered lattices [29].

Since the mechanism of universal localization relies only on (i) a staggered or sublattice-asymmetric drive and (ii) a bounded on-site modulation, it is directly realizable in multiple experimental platforms. In ultracold atoms, driven Aubry–André and generalized quasiperiodic lattices have been implemented with high control [30, 31], while periodically modulated tunneling can be engineered via lattice shaking or Raman-assisted tunneling [24]. Photonic waveguide arrays provide an alternative platform where longitudinal modulation implements Floquet driving and quasiperiodic refractive-index patterns realize the AA potential [32]. All these platforms can measure participation ratios, wave-packet spreading, and energy absorption, making the predicted localization plateau immediately testable.

Our results therefore establish emergent non-perturbative Floquet localization as a physically robust phenomenon, detectable in existing experiments with imprints captured by superasymptotically truncated perturbation theory. This interplay between rare resonances, asymptotic expansions, and exact localization opens a new direction for exploring controllable non-perturbative phases in driven quantum systems.

Acknowledgments S. S. and S. P. acknowledges fruitful discussions with Krishnendu Sengupta and Arnab Das. All authors acknowledge early collaborations with Hrithik Nandy. S. S. acknowledges support from the Anusandhan National Research Foundation (Department of Science and Technology) Govt. of India, under grant no. CRG/2023/007457 and an internal grant from the Indian Institute of Science Education and Research, Tirupati. A. R. acknowledges support from IIT Hyderabad, India through the Seed Grant SG/IITH/F337/2023-24/SG-175, and ANRF (DST), Govt. of India under the grant no. ANRF/IRG/2024/001653/PS.

[1] P. W. Anderson, Absence of diffusion in certain random lattices, *Phys. Rev.* **109**, 1492 (1958).

[2] R. Ducazez and F. Huveneers, Anderson localization for periodically driven systems, *Annales Henri Poincaré* **18**, 2415 (2017).

[3] D. F. Martinez and R. A. Molina, Delocalization induced by low-frequency driving in disordered tight-binding lattices, *Phys. Rev. B* **73**, 073104 (2006).

[4] D. H. Dunlap and V. M. Kenkre, Dynamic localization of a charged particle moving under the influence of an electric field, *Phys. Rev. B* **34**, 3625 (1986).

[5] M. Holthaus, G. H. Ristow, and D. W. Hone, ac-field-controlled anderson localization in disordered semiconductor superlattices, *Phys. Rev. Lett.* **75**, 3914 (1995).

[6] P. Dotti, Y. Bai, T. Shimasaki, A. R. Dardia, and D. M. Weld, Measuring a localization phase diagram controlled by the interplay of disorder and driving, *Phys. Rev. Res.* **7**, L022026 (2025).

[7] T. Shimasaki, Y. Bai, H. E. Kondakci, P. Dotti, J. E. Pagett, A. R. Dardia, M. Prichard, A. Eckardt, and D. M. Weld, Reversible phasonic control of a quantum phase transition in a quasicrystal, *Phys. Rev. Lett.* **133**, 083405 (2024).

[8] A. Richardella, P. Roushan, S. Mack, B. Zhou, D. A. Huse, D. D. Awschalom, and A. Yazdani, Visualizing critical correlations near the metal-insulator transition in $ga_{1-x} mn_{x}as$, *Science* **327**, 665 (2010), <https://www.science.org/doi/pdf/10.1126/science.1183640>.

[9] J. Billy, V. Josse, Z. Zuo, A. Bernard, B. Hambrecht, P. Lugan, D. Clément, L. Sanchez-Palencia, P. Bouyer, and A. Aspect, Direct observation of anderson localization of matter waves in a controlled disorder, *Nature* **453**, 891 (2008).

[10] G. Semeghini, M. Landini, P. Castilho, S. Roy, G. Spagnoli, A. Trenkwalder, M. Fattori, M. Inguscio, and G. Modugno, Measurement of the mobility edge for 3d anderson localization, *Nature Physics* **11**, 554 (2015).

[11] A. Eckardt and E. Anisimovas, High-frequency approximation for periodically driven quantum systems from a floquet-space perspective, *New Journal of Physics* **17**, 093039 (2015).

[12] D. A. Abanin, W. De Roeck, W. W. Ho, and F. m. c. Huveneers, Effective hamiltonians, prethermalization, and slow energy absorption in periodically driven many-body systems, *Phys. Rev. B* **95**, 014112 (2017).

[13] S. Aditya, K. Sengupta, and D. Sen, Periodically driven model with quasiperiodic potential and staggered hopping amplitudes: Engineering of mobility gaps and multifractal states, *Phys. Rev. B* **107**, 035402 (2023).

[14] P. S. Nair, D. Joy, R. Deb, S. Pakrashi, and S. Sanyal, Emergent scale and anomalous dynamics in certain nearest-neighbor quasiperiodic tight binding models in one dimension, *Phys. Rev. B* **112**, 104203 (2025).

[15] S. Aubry and G. Andre, Analyticity breaking and anderson localization in incommensurate lattices, *Ann. Israel Phys. Soc* **3**, 18 (1980).

[16] T. Kohlert, S. Scherg, X. Li, H. P. Lüschen, S. Das Sarma, I. Bloch, and M. Aidelsburger, Observation of many-body localization in a one-dimensional system with a single-particle mobility edge, *Phys. Rev. Lett.* **122**, 170403 (2019).

[17] Y. Wang, J.-H. Zhang, Y. Li, J. Wu, W. Liu, F. Mei, Y. Hu, L. Xiao, J. Ma, C. Chin, and S. Jia, Observation of interaction-induced mobility edge in an atomic aubry-andré wire, *Phys. Rev. Lett.* **129**, 103401 (2022).

[18] A. Iserles and S. P. Nørsett, On the solution of linear differential equations in lie groups, *Philosophical Transactions of the Royal Society of London. Series A: Mathematical, Physical and Engineering Sciences* **357**, 983 (1999).

[19] S. Blanes, F. Casas, J.-A. Oteo, and J. Ros, The magnus expansion and some of its applications, *Physics reports* **470**, 151 (2009).

[20] T. Liu and H. Guo, Mobility edges in off-diagonal disordered tight-binding models, *Phys. Rev. B* **98**, 104201 (2018).

[21] M. Rodriguez-Vega, M. Lentz, and B. Seradjeh, Floquet perturbation theory: formalism and application to low-frequency limit, *New Journal of Physics* **20**, 093022 (2018).

[22] S. Klarsfeld and J. A. Oteo, Recursive generation of higher-order terms in the magnus expansion, *Phys. Rev. A* **39**, 3270 (1989).

[23] M. Bukov, L. D’Alessio, and A. Polkovnikov, Universal high-frequency behavior of periodically driven systems: from dynamical stabilization to floquet engineering, *Advances in Physics* **64**, 139 (2015), <https://doi.org/10.1080/00018732.2015.1055918>.

[24] N. Goldman and J. Dalibard, Periodically driven quantum systems: Effective hamiltonians and engineered gauge fields, *Phys. Rev. X* **4**, 031027 (2014).

[25] T. Mori, T. Kuwahara, and K. Saito, Rigorous bound on energy absorption and generic relaxation in periodically driven quantum systems, *Phys. Rev. Lett.* **116**, 120401 (2016).

[26] T. Kuwahara, T. Mori, and K. Saito, Floquet-magnus theory and generic transient dynamics in periodically driven many-body quantum systems, *Annals of Physics* **367**, 96 (2016).

[27] M. M. Maricq, Application of average hamiltonian theory to the nmr of solids, *Phys. Rev. B* **25**, 6622 (1982).

[28] T. Haga, Divergence of the floquet-magnus expansion in a periodically driven one-body system with energy localization, *Phys. Rev. E* **100**, 062138 (2019).

[29] S. Pakrashi, A. Rajak, and S. Sanyal, (in preparation).

[30] G. Roati, C. D’Errico, L. Fallani, M. Fattori, C. Fort, M. Zaccanti, G. Modugno, M. Modugno, and M. Inguscio, Anderson localization of a non-interacting bose-einstein condensate, *Nature* **453**, 895 (2008).

[31] M. Schreiber, S. S. Hodgman, P. Bordia, H. P. Lüschen, M. H. Fischer, R. Vosk, E. Altman, U. Schneider, and I. Bloch, Observation of many-body localization of interacting fermions in a quasirandom optical lattice, *Science* **349**, 842 (2015), <https://www.science.org/doi/pdf/10.1126/science.aaa7432>.

[32] Y. Lahini, R. Pugatch, F. Pozzi, M. Sorel, R. Morandotti, N. Davidson, and Y. Silberberg, Observation of a localization transition in quasiperiodic photonic lattices, *Phys. Rev. Lett.* **103**, 013901 (2009).

END MATTER

I. EXACT METHOD

We divide the time period T into N Trotter steps, where N is chosen to be large enough such that $H(t)$ does not change significantly between t_s and $t_{s+T/N}$ for any time instant t_s . Then we construct the stroboscopic time evolution operator $U(T, 0) = \prod_{s=1}^N \sum_n e^{-i\epsilon_n^s \frac{T}{N}} |\psi_n^s\rangle\langle\psi_n^s|$ using the Suzuki-Trotter decomposition, where ϵ_n^s and $|\psi_n^s\rangle$ are the eigenvalues and eigenvectors of the instantaneous Hamiltonian $H(t_s)$ on a lattice of size L , $H(t_s)|\psi_n^s\rangle = \epsilon_n^s |\psi_n^s\rangle$. Finally, we obtain the stroboscopic Floquet eigenstates, $|\chi_m\rangle$ and eigenvalues, E_m^F by diagonalizing the unitary matrix $U(T, 0)$, which satisfies $U(T, 0)|\chi_m\rangle = e^{-iE_m^F t}|\chi_m\rangle$. The corresponding Floquet Hamiltonian is given by $H_F = \sum_m E_m^F |\chi_m\rangle\langle\chi_m|$.

II. FLOQUET PERTURBATION THEORY

In FPT one considers the time-dependent part of the Hamiltonian as the unperturbed Hamiltonian and the static part of the Hamiltonian as the perturbation. The central idea is to construct the Floquet states in the presence of weak static perturbation from the known unperturbed floquet states by applying the time-dependent perturbation theory. The perturbation theory converges when the amplitude of the drive a is larger than the amplitudes of all static terms γ , and λ .

In order to develop FPT for our model, we rewrite the Hamiltonian as follows: $H_{FPT}(t) = H_0(t) + V_1 + V_2$ and took Fourier transformation which takes $c_{i,A} \rightarrow a_k, c_{i,A}^\dagger \rightarrow a_k^\dagger$ and $c_{i,B} \rightarrow b_k, c_{i,B}^\dagger \rightarrow b_k^\dagger$. This yields zeroth order term in k -space as

$$H_0(t) = \sum_k [a \sin(\omega t)(1 - e^{-2ik})a_k^\dagger b_k + a \sin(\omega t)(1 - e^{2ik})b_k^\dagger a_k], \quad (5)$$

and the perturbation terms as

$$V_1 = \sum_k [\gamma(1 + e^{-2ik})a_k^\dagger b_k + h.c.], \quad (6)$$

$$\text{and } V_2 = \sum_k [f_1(k, k')a_k^\dagger a_{k'} + f_1(k, k')b_k^\dagger b_{k'}], \quad (7)$$

where $f_1(k, k') = \sum_j \frac{2\lambda}{L} \cos(2\pi\alpha(2j))e^{2i(k-k')j}$ and $f_2(k, k') = \sum_j \frac{2\lambda}{L} \cos(2\pi\alpha(2j+1))e^{2i(k-k')j}$, $k \in [-\frac{\pi}{2}, \frac{\pi}{2}]$. Now, if we redefine our basis states as $|k \uparrow\rangle = a_k^\dagger |0\rangle$ and $|k \downarrow\rangle = b_k^\dagger |0\rangle$, the eigenstates of H_0 can be expressed as $|k+\rangle = \frac{1}{\sqrt{2}}(|k \uparrow\rangle - ie^{ik}|k \downarrow\rangle)$ and $|k-\rangle = \frac{1}{\sqrt{2}}(|k \uparrow\rangle + ie^{ik}|k \downarrow\rangle)$, in this basis the Hamiltonian can be written in terms of Pauli matrices. The first-order correction term arising from V_1 in $|k\pm\rangle$ is given by:

$$H_{F1}^{(1)} = \frac{1}{2} \sum_k \psi_k^\dagger \begin{pmatrix} 2\alpha_{2k} & \alpha_{1k} \\ \alpha_{1k}^* & -2\alpha_{2k} \end{pmatrix} \psi_k \quad (8)$$

Where,

$$\alpha_{2k} = -2\gamma J_0(\mu_k) \cos(k) \sin(\mu_k) \quad (9)$$

$$\alpha_{1k} = \gamma J_0(\mu_k) \cos(\mu_k) (1 + e^{-2ik}) \quad (10)$$

We use a two-component operator $\psi_k = (a_k, b_k)$ and $\mu_k = \frac{4\alpha \sin(k)}{\omega}$. Similarly, first order correction term $H_{F2}^{(1)}$, arising from V_2 .

$$\begin{aligned} H_{F2}^{(1)} = & \sum_k \frac{1}{2} [(X + \tilde{X} + Y + \tilde{Y})a_k^\dagger a_{k'} \\ & + e^{i(k-k')}(X + \tilde{X} - Y - \tilde{Y})b_k^\dagger b_{k'} \\ & + ie^{-ik'}(X - \tilde{X} - Y + \tilde{Y})a_k^\dagger b_{k'} \\ & - ie^{ik}(X - \tilde{X} + Y - \tilde{Y})b_k^\dagger a_{k'}] \end{aligned} \quad (11)$$

Where, $X = e^{i\mu_{kk'}^-} J_0(\mu_{kk'}^-) P_+(k, k')$, $Y = e^{i\mu_{kk'}^+} J_0(\mu_{kk'}^+) P_-(k, k')$, $\tilde{X} = e^{-i\mu_{kk'}^-} J_0(\mu_{kk'}^-) P_+(k, k')$, $\tilde{Y} = e^{-i\mu_{kk'}^+} J_0(\mu_{kk'}^+) P_-(k, k')$. Where, $P_+(k, k') = \frac{1}{2}(f_1(k, k') + f_2(k, k')e^{i(k-k')})$, $P_-(k, k') = \frac{1}{2}(f_1(k, k') - f_2(k, k')e^{i(k-k')})$, $\mu_{kk'}^+ = \frac{\mu_k + \mu_{k'}}{2}$ and $\mu_{kk'}^- = \frac{\mu_k - \mu_{k'}}{2}$. Finally, we perform Inverse Fourier Transformation of $H_F = H_{F1}^{(1)} + H_{F2}^{(1)}$ to obtain approximated real space Hamiltonian.

SUPPLEMENTARY MATERIAL

1. Analysis by Exact Method

a. Points outside the universal localization region

Using an exact numerical approach, we study few points away from the universal localization region for $\lambda = 1$ of the AA model, where the static model has completely delocalized spectrum. We plot the probability profile (light cone) $p(nT, j) = |\psi_{nT}(j)|^2$ and the RMS spread of the wave packet $\sigma(n) = \sqrt{\sum_j (j - j_0)^2 |\psi_{nT}(j)|^2}$ in Figs. 3(a), 3(b) and 3(c) for $(a, \omega) = (0.1, 2.45), (3.5, 2.45)$ and $(2.15, 3.5)$ respectively. For each of these points we find signatures of ballistic transport, where $p(nT, j)$ rapidly spreads across the system and reaches the boundary within $\sim 100n - 200n$ cycles. This signature of early time boundary-hitting is consistent with σ vs. n plots in 3(d), showing $\eta \approx 1$, where $\sigma \sim n^\eta$.

b. Weak disorder cases

In Figs. 3(e) and 3(f) we study $\lambda \rightarrow 0$, here we plot the state resolved IPR for different drive protocol and show that the system remains localized, as $\mathcal{O}(1)$ IPR scaling persists even in weak disorder strength $\lambda = 0.5, 0.1$. This demonstrates how the universal localization arises as the interplay between disorder and drive, we also find the universal localization phenomena to complete disappear at $\lambda = 0$. However, the universal localization region in Fig. 1(a) effectively collapses to a point if λ is decreased significantly. Nevertheless, the slow transport behavior of localized regime is clearly noticeable even at such weak disorder $\lambda = 0.5$. Figs. 3(g) and 3(h) demonstrate the slow transport.

2. Analysis by Floquet Perturbation Theory

Performing a numerical Inverse Fourier Transformation (IFT) of the momentum space Hamiltonian reveals that $H_{F1}^{(1)}$ contributes predominantly to off-diagonal terms, while $H_{F2}^{(1)}$ generates both diagonal and off-diagonal components. The relative weight of diagonal to off-diagonal terms determines the nature of the phase at a given (a, ω) . We show

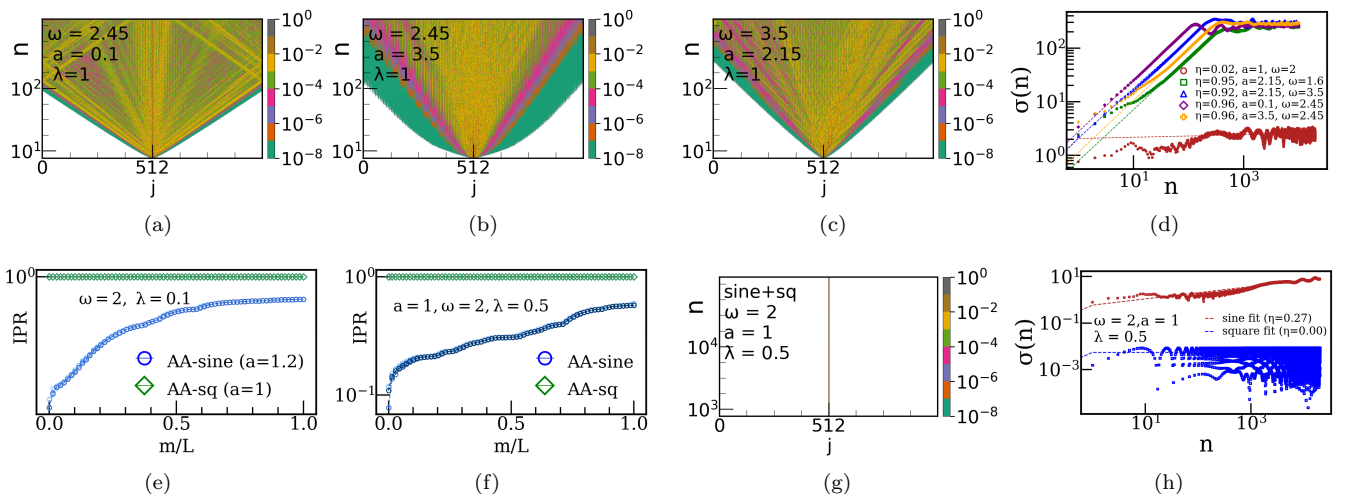


FIG. 3: a)-c) Rapid wave packet spreading observed for the points lying outside universal localization $(a, \omega) = (0.1, 2.45), (3.5, 2.45)$ and $(2.15, 3.5)$ at $\lambda = 1$, indicating ballistic transport with scaling exponent $\eta \approx 1$ as quantified in d). Here, $L = 1024$, $N = 1000$ and sine drive used for the analysis. e) IPR scaling plotted for $\lambda = 0.1$, demonstrating drive-induced universal localization for weak disorder. Plots f)-g) illustrate localized scaling in the form of IPR and slow wave packet evolution in the form of $\sigma(n)$ and wave packet profile using geometric mean of square and sine drive, proving the existence of universal localization. $L = 500, 1000, 1500, 2000$ is used for scaling and $L = 1024$ for transport.

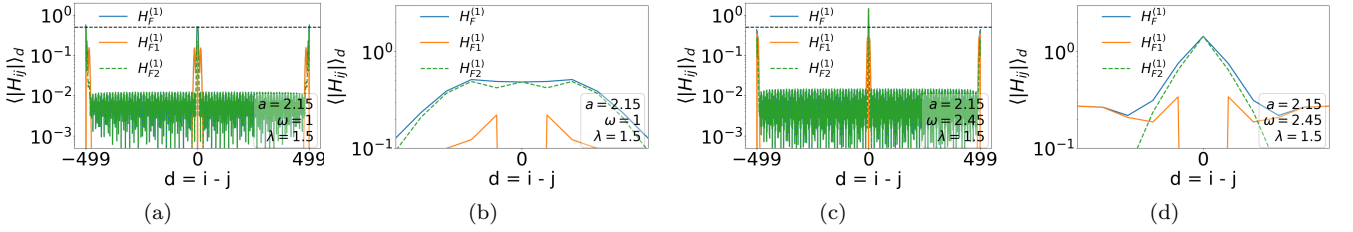


FIG. 4: **a),b)** The combined effect of $H_{F1}^{(1)}$ and $H_{F2}^{(1)}$ decreases the diagonal weight relative to off-diagonals at $(a, \omega) = (2.15, 1)$, resulting in delocalization. Whereas, **c),d)** $(a, \omega) = (2.15, 2.45)$ shows enhanced diagonal weight leading to localization. Here, $L = 500$ and sine drive is implemented.

here that after IFT, the Floquet Hamiltonian at $(a, \omega) = (2.15, 2.45)$ exhibits enhanced diagonal weight leading to localization. We plot the average matrix element value $\langle |H_{ij}| \rangle_d$ vs. distance from the diagonal $d = |i - j|$ in Fig. 4(c), in Fig. 4(d) we zoom near the diagonal($d = 0$). In contrast, for $(a, \omega) = (2.15, 1)$, we plot the same average matrix element in Fig. 4(a) and zoomed near the diagonal in Fig. 4(b), from these figures we see a dominant off-diagonal contribution leading to delocalization.

3. Analysis by Van Vleck perturbation theory

a. Analysis of resonances in VVPT

We consider the Fourier representation $H(t) = \sum_p H_p e^{ip\omega t}$, where the H_0 represents the static part of the Hamiltonian and the remaining harmonics represent time dependent part of the drive. In the interaction picture we can define, $V_I(t) = e^{iH_0 t}(H(t) - H_0)e^{-iH_0 t}$ and $U_I(T) = I + S_I^{(1)}(T) + S_I^{(2)}(T)$. The first-order contribution in the Dyson series is $S_I^{(1)}(T) = \int_0^T dt V_I(t)$ in the eigenbasis of H_0 is, $\langle w | S_I^{(1)}(T) | x \rangle = \int_0^T dt \langle w | e^{iH_0 t} H(t) e^{-iH_0 t} | x \rangle$. Using the Fourier expansion of $H(t)$ and eigenvalue equation for $H_0 |x\rangle = E_x |x\rangle$, the integrand becomes $\langle w | e^{iH_0 t} H(t) e^{-iH_0 t} | x \rangle = \langle w | H(t) e^{i(E_w - E_x + p\omega)} | x \rangle$. The time integral therefore generates denominators of the form $(E_w - E_x + p\omega)^{-1}$. However, the explicit prefactor $\frac{1}{T}$ appearing in the definition of H_{eff} ($H_{eff} = \frac{1}{T} \ln(U)$) ensures that the contribution is of order $1/\omega^0$. Similarly, $S_I^{(2)}(T) = -\frac{1}{2} \int_0^T dt_1 \int_0^{t_1} dt_2 [V_I(t_1), V_I(t_2)]$. After evaluating the nested time integrals and explicit division by T yields a leading order correction term which represents $O(\omega^{-1})$ process $H_{VV}^{(1)}$. This contains denominators of the form $(E_w - E_x + p_1\omega + p_2\omega)^{-1}$, $(E_w - E_x + p_1\omega)^{-1}$ and $(E_w - E_x + p_2\omega)^{-1}$. From this analysis, the allowed range of photon numbers m can be inferred at a given perturbative order. As we see in $H_{VV}^{(1)}$ for sine drive m can take values from $[-2, -1, 0, 1, 2]$ as both $p_1, p_2 = \pm 1$. More generally, the range for allowed m values for any perturbation order n will be from $-(n+1)$ to $n+1$. So, with this modified range we redefined our resonance diagnostic $\mathcal{R}_\nabla = \frac{|\langle w | H^{(2k)} | x \rangle|}{\min(|E_w^0 - E_x^0 \pm m\omega|)}$, where $m \in [-(2k+1), 2k+1]$. We quantify the count of such resonance instances whenever $\mathcal{R}_\nabla > 1$ and also check the magnitude by computing the average value of all \mathcal{R}_∇ s. As shown in fig. 5(a), the number of resonance counts is high and increases by orders of magnitude with perturbative order $2k$ for intermediate disorder strengths $\lambda = 1, 1.5$, indicating a resonance-dominated spectrum. However, we find in fig. 5(b) and fig. 5(c) that with increased λ and $2k$, the average and rms \mathcal{R}_∇ attains a maximum value, indicating that resonances are sparse but progressively stronger for such cases (In practice, such rare resonance condition are not achieved as for high λ s optimal truncation order is $2k \approx 6$). In contrast, for intermediate λ , the number of resonant events increases substantially, implying that a larger fraction of effective Hamiltonian elements are affected by resonances (for $\lambda = 1$, the average and rms \mathcal{R}_∇ attains a high value), which causes breakdown of agreement with exact numerics (specifically for $\lambda=1$ case).

b. Convergence analysis of VVPT using ratio test with different norms

We introduce three kinds of ratio test protocols to determine the optimal truncation order of the VVPT. In each case, the ratio test is either defined by the matrix element (denoted by $H_{i,j}$) or eigenvalue of H_{eff} at each $\mathcal{O}(2k)$, which essentially represents the underlying $\bar{R}_{i,j}^{2k}$. We define,

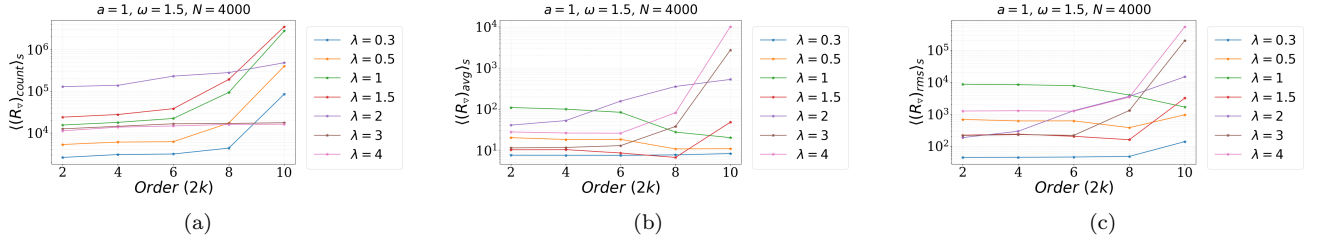


FIG. 5: **a)** The count of resonance \mathcal{R}_∇ is high and grows moderately with increasing order $2k$ at intermediate $\lambda = 1, 1.5$. **b),c)** At higher λ , resonances are fewer but stronger, reflected in the form of average and rms \mathcal{R}_∇ strength, while $\lambda = 1$ contains a consistent high \mathcal{R}_∇ average and rms in initial orders proving the breakdown of perturbation at this size $L = 4000$. Here, $a = 1$ and $\omega = 1.5$; sine drive is used for calculation.

1. $avg_H = \bar{R}^{2k+2}/\bar{R}^{2k}$, where $\bar{R}^{2k} = \langle |\bar{R}_{i,j}^{2k}| \rangle = \frac{\sum_{i,j: H_{ij} \neq 0} |H_{ij}|}{N_{nz}}$.
2. $rms_H = R_{rms}^{2k+2}/R_{rms}^{2k}$, where $R_{rms}^{2k} = \left[\sqrt{\frac{1}{N_{nz}} \sum_{i,j \in \text{nonzero}} (R_{i,j})^2} \right]_{2k} = \left[\sqrt{\frac{1}{N_{nz}} \sum_{i,j \in \text{nonzero}} (H_{i,j})^2} \right]_{2k}$.
3. $norm_H = |R^{2k+2}|_2/|R^{2k}|_2$, where $|R^{2k}|_2 = \left[\|H\|_2 \right]_{2k}$, i.e. the spectral norm.

Here, N_{nz} denotes the number of nonzero matrix elements (amplitude strength $\geq 10^{-8}$) of the effective Hamiltonian (H) at a given order $2k$. We found three ratio tests capture distinct aspects of effective H . The quantity avg_H reflects overall growth of matrix elements $H_{i,j}$ when higher order correction terms are included. In contrast, rms_H amplifies the presence of strong couplings both in hoppings and onsite terms. While spectral norm ($norm_H$) represents the largest eigenvalue associated with the strongest $i - j$ couplings. In this letter, we primarily rely on avg_H , which enables us to incorporate maximum permissible perturbative order, avoiding divergences of the effective H . This criterion also ensures the resulting truncated expansion remains in closest agreement with exact numerics, beyond which the perturbative series fails to provide meaningful results. In figures 6(a)-6(d), 6(e)-6(h) and 6(i)-6(l), we illustrated the avg_H , rms_H and $norm_H$ results respectively, for various L given in the main text at $a = 1, \omega = 1.5$. These plots demonstrate how avg_H allows us to access higher order perturbation expansion, as $\bar{R}^{2k+2}/\bar{R}^{2k} < 1$ for increasingly large $2k$ compared to $rms_H, norm_H$. Here $\langle \dots \rangle_s$ represents the sample average over different random number sequences. The same analysis is shown for a non-universal $a = 5, \omega = 7.1$ in figures 6(m)-6(x) and the corresponding $|H_{i,j}|$ and $|E|$ eigenvalue distributions are given in plots 7(a)-7(t) and 8(a)-8(t) for $(a, \omega) = (1, 1.5)$ and $(5, 7.1)$, respectively. The $|H_{i,j}|$ distributions clearly show that inclusion of higher order perturbative terms generates both a high-end tail (HET) with $|H_{i,j}| > 10^0$ and a low-end tail (LET) with weights $< 10^{-3}$. The plots show that $|E|$ has greater sensitivity towards strong couplings as the eigenvalue spectrum develops a tail at HET, which grows monotonically with $|H_{i,j}|$ s of higher order. This behavior also explains why $a = 5, \omega = 7.1$ remains well behaved across all ratio tests, unlike $a = 1, \omega = 1.5$; as the former develops a broader LET compared to its HET, effectively suppressing the emergence of large matrix elements and promoting divergence at higher order. The reason for such behavior is that the latter is closer to the radius of convergence compared to the former one, which in turn promotes divergence at early orders of perturbation theory.

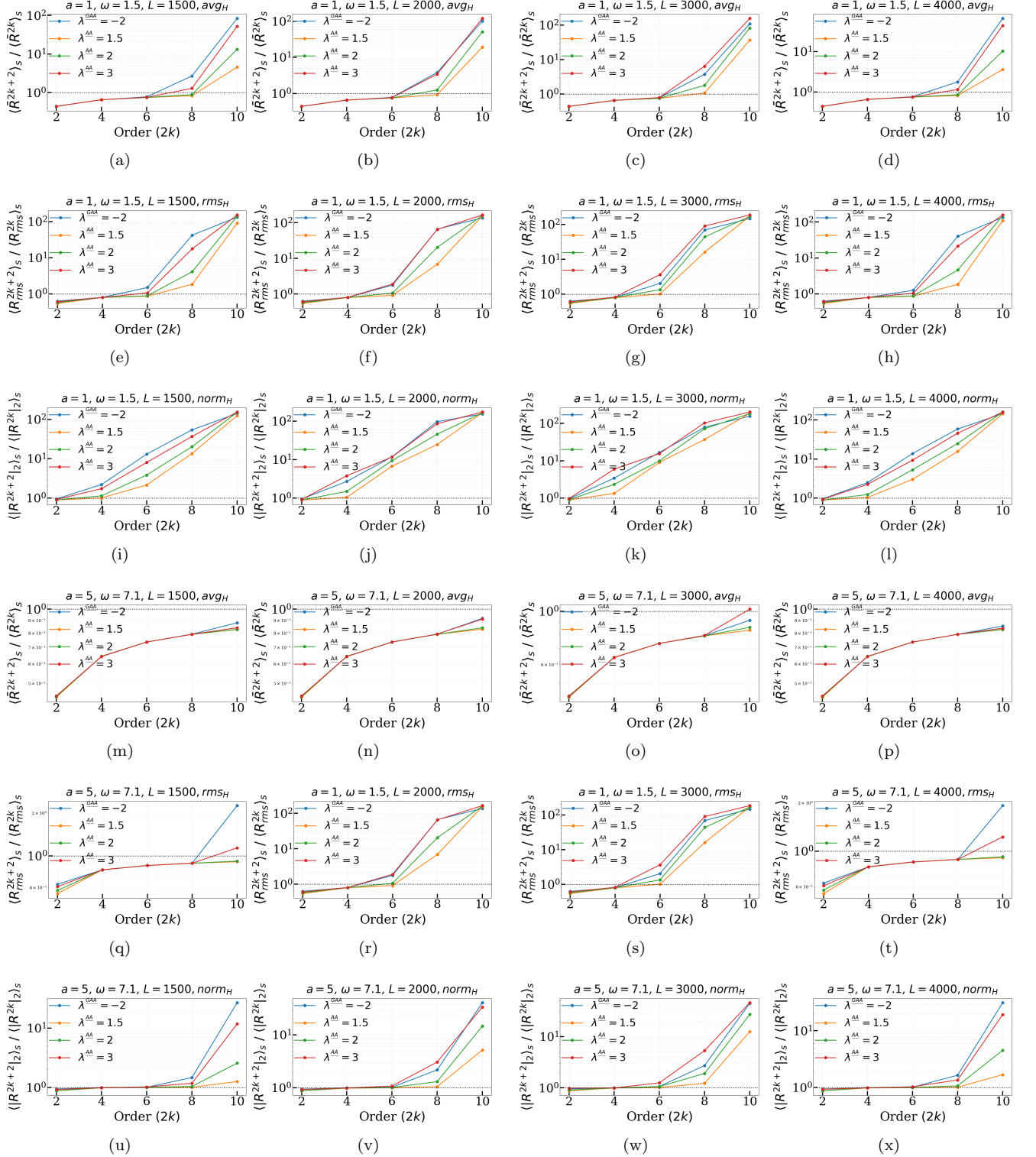


FIG. 6: **a)-d)**Ratio test results for heuristic n^{th} -order VVPT using avg_H for system sizes $L = 1500, 2000, 3000$ and 4000 at $(a, \omega) = (1, 1.5)$ shown for AA potentials with $\lambda = 1.5, 2, 3$ and for GAA model with $\lambda = -2, \beta = 0.5$. The same parameters are used to compute rms_H and $norm_H$ in **e)-h)** and **i)-l)** respectively. Panel **m)-p)**, **q)-t)** and **u)-x)** show the corresponding analysis of avg_H , rms_H and $norm_H$ for $(a, \omega) = (5, 7.1)$. From this analysis of avg_H across orders, we provide a criterion for selecting the optimal truncation order of the perturbation expansion.

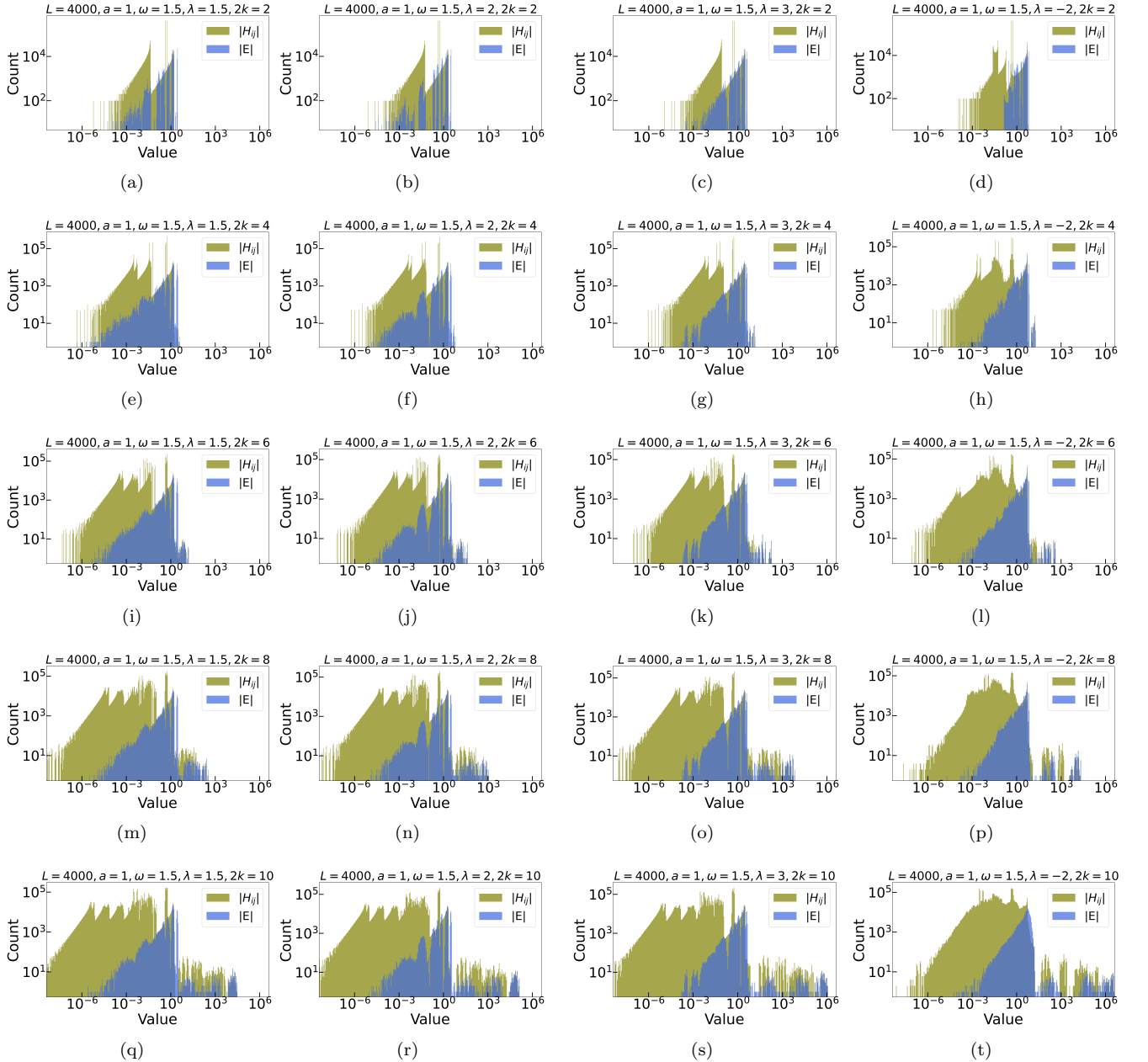


FIG. 7: a)-d) Represents matrix element distributions $|H_{i,j}|$ and eigenvalue distributions $|E|$ for the AA model with $\lambda = 1.5, 2, 3$ and the GAA model with $\lambda = -2, \beta = 0.5$, evaluated at $(a, \omega) = (1, 1.5)$ and lower order $2k = 2$. Panels e)-h), i)-l), m)-p) and q)-t) show the corresponding distributions after including higher order corrections $2k = 4, 6, 8$ and 10 respectively to the second order effective Hamiltonian. As $2k$ increases, the $|H_{i,j}|$ distribution develops a pronounced HET and LET. It is evident the $|E|$ distribution is significantly more sensitive to HET, exhibiting a monotonic growth in its tail consistent with the increase in large $|H_{i,j}|$ elements of H_{eff} .

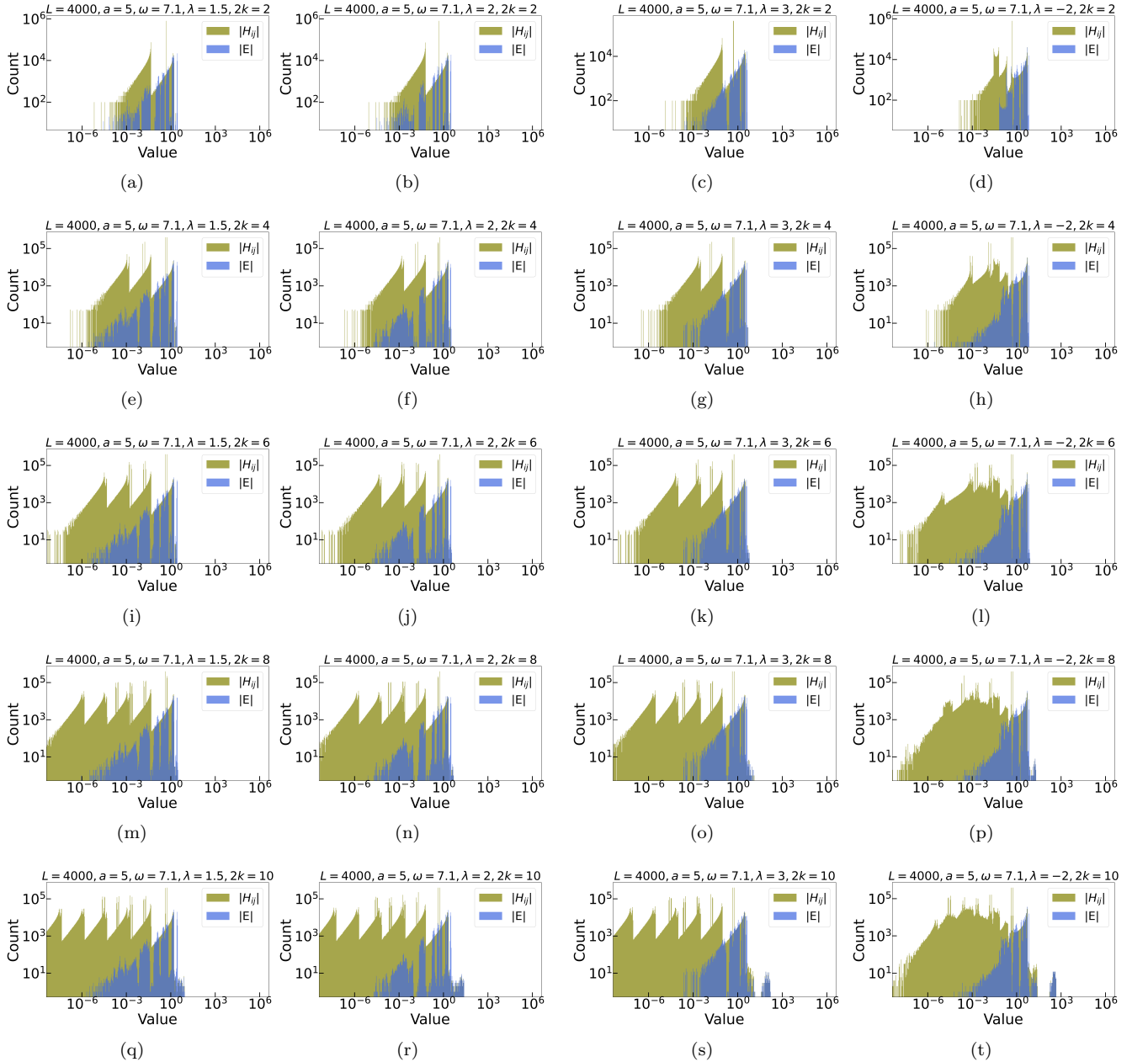


FIG. 8: a)-d) Represents matrix element distributions $|H_{i,j}|$ and eigenvalue distributions $|E|$ for the AA model with $\lambda = 1.5, 2, 3$ and the GAA model with $\lambda = -2, \beta = 0.5$, evaluated at $(a, \omega) = (5, 7.1)$ and lower order $2k = 2$. Panels e)-h), i)-l), m)-p) and q)-t) show the corresponding distributions after including higher order corrections $2k = 4, 6, 8$ and 10 respectively to the second order effective Hamiltonian. As $2k$ increases, the $|H_{i,j}|$ distribution develops a pronounced HET and LET. It is evident the $|E|$ distribution is significantly more sensitive to HET, exhibiting a monotonic growth in its tail consistent with the increase in large $|H_{i,j}|$ elements of H_{eff} .